Advanced Powder Technology 28 (2017) 1745–1759

Contents lists available at ScienceDirect

Advanced Powder Technology

journal homepage: www.elsevier.com/locate/apt

Original Research Paper

Discrete element modeling and experimental investigation of hot pressing of intermetallic NiAl powder

Szymon Nosewicz [a,*], Jerzy Rojek [a], Marcin Chmielewski [b], Katarzyna Pietrzak [a,b]

[a] Institute of Fundamental Technological Research Polish Academy of Sciences, Pawińskiego 5B, 02-106 Warsaw, Poland
[b] Institute of Electronic Materials Technology, Wólczyńska 133, 01-919 Warsaw, Poland

ARTICLE INFO

Article history:
Received 26 July 2016
Received in revised form 4 April 2017
Accepted 20 April 2017
Available online 4 May 2017

Keywords:
Powder metallurgy
Hot pressing
Sintering
Simulation
Discrete element method
Nickel aluminide

ABSTRACT

This paper presents the numerical and experimental analysis of hot pressing of NiAl powder with an emphasis on the best possible representation of its main stages: initial powder compaction and pressure-assisted sintering. The numerical study has been performed within the discrete element framework. In the paper, an original viscoelastic model of hot pressing has been used. In order to ensure that the applied values of material parameters in numerical simulations are appropriate, the reference literature has been reviewed. It produced the relations and equations to estimate the values of all required sintering material parameters of the considered viscoelastic model. Numerical simulations have employed the geometrical model of the initial dense specimen generated by a special algorithm which uses the real grain distribution of powder. The numerical model has been calibrated and validated through simulations of the real process of hot pressing of intermetallic NiAl material. The kinetics of compaction, sintering and cooling stage indicated by the evolution of density, shrinkage and densification rate have been studied. The comparison of numerical and experimental results has shown a good performance of the developed numerical model.

1. Introduction

Uniaxial hot pressing is a common technology of powder metallurgy integrating the processes of powder compaction and sintering. Hot pressing is mostly used to manufacture hard and brittle materials, such as ceramics, intermetallics and metal matrix composites, where a high density must be guaranteed. In this manufacturing technique, powder material is converted into a polycrystalline solid body in a die under the combined action of pressure and heat (Fig. 1).

Typical pressure and temperature profiles in the hot pressing process are shown in Fig. 2. At the beginning of the process the external pressure is applied and the initial powder compaction occurs to form a green body (an unsintered specimen). Applied pressure improves particle rearrangement and bulk density and reduces porosity. These factors are favorable for subsequent sintering, since the diffusion path during sintering process are reduced, and as a consequence of that, a lower temperature and shorter time are required.

As a next step, the material is heated up to a certain elevated temperature T_s and held for a certain time t_s. Temperature activation indicates the start of the sintering process which is the most important stage of hot pressing process. It involves further consolidation of initially compacted powder due to the mass transport mechanism. The sintering temperature T_s is usually within the range of 0.5–0.9 of the melting point. The compaction pressure in hot pressing is much lower than the pressure of conventional powder compaction, and it is usually up to 50 MPa.

A fully-dense compact material can be obtained as a result of hot pressing process. Creep and diffusion are the dominant densification mechanisms in hot pressing at high temperature. The final microstructure is the result of evolutionary changes due to particle compaction and rearrangement, the formation and growth of diffusion bonds, the shrinkage of the bulk material, grain growth, a gradual reduction and elimination of porosity.

The manufacturing process of hot pressing can be modeled as the combination of the two subsequent main stages: the initial powder compaction and pressure-assisted sintering. The powder compaction process has been modelled using mainly the continuum modelling and the discrete one. Discrete element method (DEM) is a relatively new numerical method developed intensively at present time by many investigators [1–3]. DEM is based on a

* Corresponding author.
E-mail address: snosew@ippt.pan.pl (S. Nosewicz).

http://dx.doi.org/10.1016/j.apt.2017.04.012

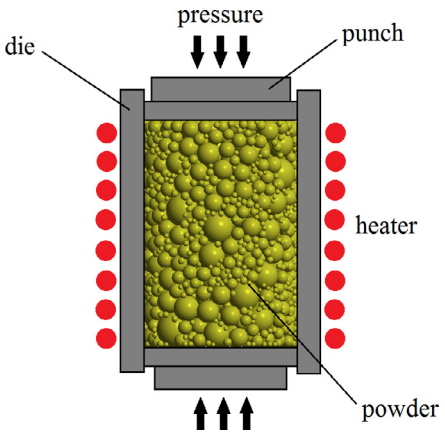

Fig. 1. Scheme of hot pressing process.

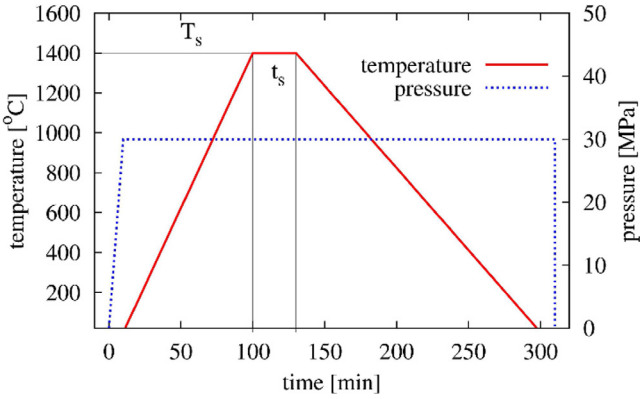

Fig. 2. Typical temperature and pressure profiles in a hot pressing process.

discrete representation of the compacted powder. Discrete element models consider the elastic (only for small pressure), elasto-plastic or plastic (large pressure) deformation of particles. The non-linear Hertz model was used in the majority of elastic or elasto-plastic models of powder compaction, for instance, in the model presented by Martin et al. [4], which considers both the elastic and plastic ranges of the contact interactions. More complicated (representing also plastic deformation) is the linear hysteretic spring model proposed by Luding [1], which is the simplest version of nonlinear-hysteretic force laws. A simple linear elastoplastic and adhesive contact model for spherical particles has been proposed by Pasha et al. [5]. Plastic deformation of contacts during loading and elastic unloading accompanied by adhesion are considered. A model assuming rigid plastic behavior according to the Hollomon stress–strain curve has been developed by Storåkers et al. [6,7].

The second and the most important stage of the hot pressing process is pressure-assisted sintering. Pressure-assisted sintering, where powder compacting and sintering occur simultaneously, is one of those techniques, which has recently become common. Generally, the sintering of granular material is a very complex process, affected by many factors, and therefore it is difficult for modelling. Recently, sintering models have been successfully implemented within the discrete element method. The quasi-static formulation of the lattice type discrete element model has been implemented by Parhami and McMeeking [8] to study the free and pressure-assisted sintering. This numerical model, based on the two-particle sintering model derived by Coble [9], was suitable only for modeling small systems. Furthermore, it did not enable new contacts to be detected and particle coarsening was not introduced. The idea of Parhami and McMeeking have been transferred to the dynamic formulation of DEM by Martin et al. [10] to study free sintering. The Authors found good agreement between simulations of copper powders and experimental data and introduced a grain-coarsening scheme. A similar model has been applied by Henrich et al. [11] to simulate the free and pressure-assisted solid-state sintering of powders with special attention to the influence of particle rearrangement during sintering. Moreover, in this paper a new method for generating a realistic initial configuration of particles was presented. The study of sintered particle rearrangement has also been performed by Martin et al. [12] using a sintering model implemented in the Non Smooth Discrete Element Method. In [13] the standard viscous model of sintering has been combined with experimental studies which provided data for calibration and validation of the model. The microstructure evolution and force distribution during solid-state sintering were studied by Wang and Chen [14] at the particle length scale for a planar layer system of copper particles. The effect of particle size distributions on sintering has been studied by Wonisch et al. [15], who proved that particle distribution in the specimen has a significant effect on the strain rates and viscosity during sintering. The same authors employed discrete element modeling to determine anisotropic constitutive parameters of sintered material as a function of density [16]. Anisotropy phenomena have been also studied by Rasp et al. [17] and Martin and Borgia [18] by a discrete simulation of sintering of thin ceramic stripes constrained by a substrate. Modeling results confirmed that the occurrence of anisotropy develops along the thickness of the substrate. Furthermore, collective particle behavior has been investigated by coupling in situ X-ray microtomography and discrete element simulation by Olmos et al. [19]. The analysis of powder rearrangement allowed Martin et al. in [20] to study the evolution of a crack both in a non-constrained and constrained sintering.

Most of the presented sintering models uses the viscous particle interaction model as the main contact interaction of powder particles during the sintering. In [21] the viscous model used by other authors has been enriched by adding a spring connected in series to the viscous rheological element. In this way elastic and viscous effects in the particle interaction during sintering are treated using the Maxwell viscoelasticity.

In spite of a great number of papers concerning the numerical analysis of the initial (cold) powder compaction or sintering stage separately, there are no discrete element simulations of the hot pressing process combining both stages within one simulation. Unlike other discrete element models focused mainly on individual stages, the present paper proposes the results from all stages of the hot pressing process, including loading, heating, pressure-assisted sintering, cooling and unloading.

The objective of the paper is to check whether it is possible to reproduce the behavior of an intermetallic NiAl powder under hot pressing using the discrete element model. The model presented in this work considers the initial compaction of powder and its further consolidation during sintering performed with an external pressure. The formulation of the hot pressing model is based on the cohesionless contact model with friction (the Kelvin-Voigt system) for the initial powder compaction stage and the viscoelastic model of sintering (the Maxwell system). In this research, both models have been extended to thermal deformations caused by thermal expansion. This feature is particularly important in the prediction of powder evolution in the terms of temperature changes during the heating and cooling stages of hot pressing. All the parameters required for the simulation of the hot pressing of the intermetallic NiAl powder have been estimated using the theoretical relationships describing the diffusion and surface energy which are the main factors influencing the

sintering. A detailed procedure to evaluate the model parameters has been presented in the appendix.

The numerical model with the theoretically predicted parameters has been validated using own experimental results. Numerical simulations have been performed for different combinations of the sintering process parameters. It has been shown that the numerical model allows us to obtain useful results characterizing the whole process, such as an initial powder compaction, densification rate during sintering and effect of thermal expansion and shrinkage during heating and cooling.

2. Experimental investigation of the hot pressing process

The main objective of experimental studies of the hot pressing process has been to obtain data for the calibration and validation of the developed numerical hot pressing model. Intermetallic nickel aluminide (NiAl) - a potential high-temperature structural material for aerospace industry - has been selected as a representative material for the present research. Specimens were manufactured from a powder delivered by the Goodfellow Company. Morphology of the NiAl powder is presented in Fig. 3a. The particle size of the starting powder was analyzed with the Clemex image analyzing system. The average Feret diameter $d_{\mathrm{NiAl}}^{\mathrm{avg}} = 9.71\ \mu\mathrm{m}$ was estimated. The particle size distribution of NiAl powder has been presented in the Fig. 3b.

In the current research, investigation of the powder compaction and sintering process (with applied external pressure) has been performed on the high-temperature press HP20-4560 Thermal Technology. The specimens were manufactured at different combinations (sets) of the following sintering process parameters - sintering temperature T_s – 1300°, 1350° and 1400 °C and external pressure p – 5 and 30 MPa (Table 1). The combinations of the sintering temperature and pressure have been associated with processes denoted with roman numbers I-VI. The processes were interrupted at different time instants (measurement points) in order to study the evolution of density and microstructure. The measurement points are marked on the plot in Fig. 4.

Three technological processes have been carried out for each measuring point (for specified technological conditions of sintering process) in order to ensure the possible best accuracy. Before the test, the temperature calibration was carried out with the use of special temperature control rings (Emco Therm). Deviation of temperature measurement was about 10 °C for specific, repeatable process conditions. Holding time at maximum temperature was measured to an accuracy of 1s, and the pressure value of 0.1 MPa. The obtained results were characterized by high reproducibility of measured density. The results are the mean of three measurements made on each of the three prepared samples. The value of the standard deviation in the extreme case was 1.2%, and decreased with the increase of the relative density of sintered materials.

At the beginning of the powder metallurgy process, temperature was increased up to the sintering temperature T_s with the heating rate of 15 °C/min for all examined cases. Specimens were kept at T_s during the interval (sintering time) t_s and cooled naturally to the room temperature. In the case of sintering time $t_s = 0$ min, the specimens were heated to the sintering temperature and immediately cooled down. The pressure was applied from the beginning of powder metallurgy process to the end of the thermal cycle.

The kinetics of sintering can be evaluated by study of the densification change in time. The sintering degree was assessed by the bulk (measured), ρ, and relative density, ρ_{rel}, defined as the ratio of the bulk density and the theoretical density for the fully dense material. Results of density measurements are given in Table 1.

Obtained results strictly refer to the mictrostructure evolution presented in Fig. 5. At the initial stage, cohesive bonds are formed between particles (Fig. 5a). When the sintering process is continued the necks between particles grow due to the mass transport (Fig. 5b). As a result of the stresses in the neck and the surface tension, the particles are attracted to each other, which leads to the shrinkage of the system. The described processes, shrinkage and mass transport are inextricably linked to the total reduction of material porosity (Fig. 5c). Further experimental studies of NiAl powder sintering in the function of different process parameters have been presented in [22], where the sintering behavior of a NiAl-Al_2O_3 composite, and its individual components sintered has been investigated separately.

The results of the present investigation provide valuable information for development of numerical model of hot pressing and sintering. The density and microstructure evolution, strictly related to sintering kinetics, are essential in calibration and validation process.

3. Numerical model of the hot pressing process

The numerical model of hot pressing has been implemented within the framework of the discrete element method. The presented model is an extension of the Authors' earlier model presented in [21]. The main assumption of the model consists in representation of the powder material subjected to hot pressing by a large collection of spherical particles. It is assumed that the collective behavior of the particle system is a result of interparticle

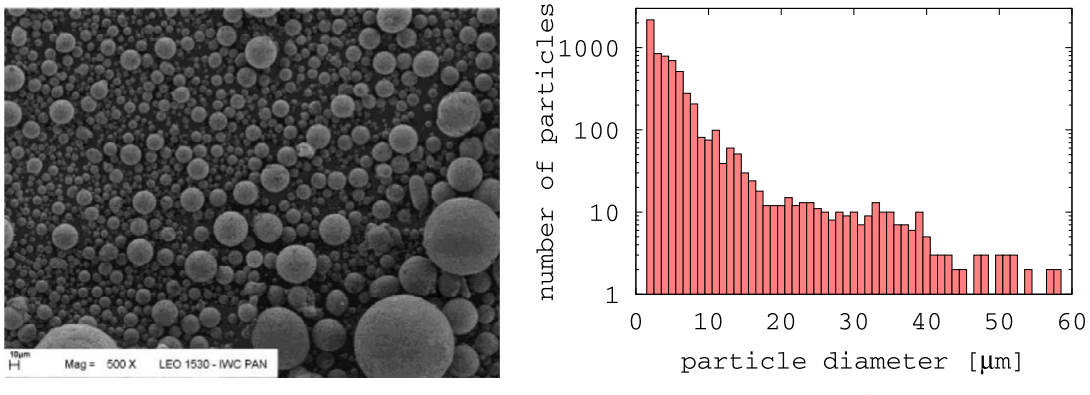

a) b)

Fig. 3. NiAl powder: (a) SEM image, (b) particle size distribution.

Table 1
Experimental density measurements for sintering of the NiAl powder.

No.	Process parameters		Density measurement point				
	T_s [°C]	p [MPa]	1	2	3	4	5
I	1400	30	5.25 (0.89)	5.35 (0.91)	5.42 (0.92)	5.78 (0.98)	5.86 (0.99)
II	1400	5	4.66 (0.79)	4.75 (0.80)	5.24 (0.89)	5.33 (0.90)	5.45 (0.92)
III	1350	30	5.25 (0.89)	5.35 (0.91)	5.52 (0.93)	5.73 (0.97)	
IV	1350	5	4.66 (0.79)	4.75 (0.80)	4.97 (0.84)	5.13 (0.87)	
V	1300	30	5.25 (0.89)	5.43 (0.92)	5.52 (0.93)		
VI	1300	5	4.66 (0.79)	4.88 (0.82)	4.90 (0.83)		

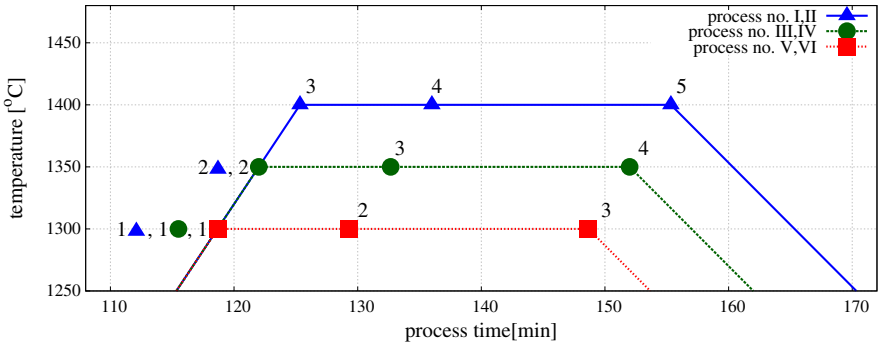

Fig. 4. Thermal profiles with density measurement points.

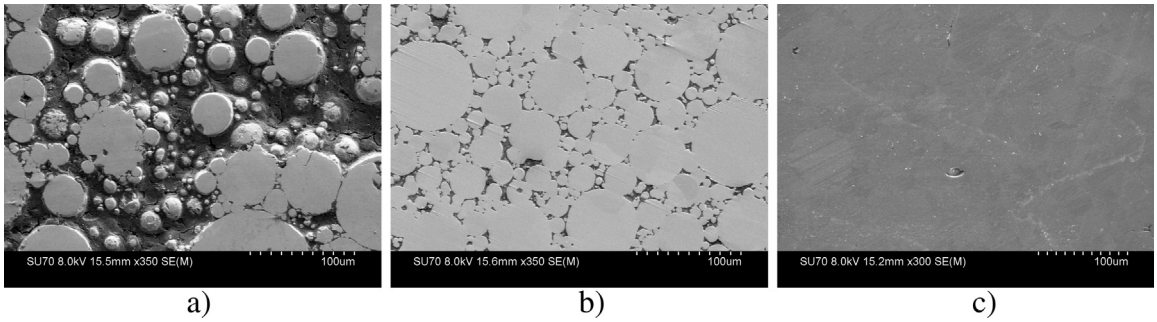

Fig. 5. SEM images of sintered NiAl material at different conditions: (a) T_s = 1300 °C, t_s = 10 min, p = 5 MPa, (b) T_s = 1400 C, t_s = 10 min, p = 5 MPa, (c) T_s = 1400 C, t_s = 30 min, p = 30 MPa.

interactions. The two-particle contact model developed in [21] takes into account different effects, including: the elasticity, contact damping and friction (for compaction), sintering driving stress and viscous (creep) flow. Here, the model has been enhanced by adding the thermal expansion. In this work, the mechanisms represented in the model enable us to simulate all the stages of the process: compaction, heating, sintering, cooling and unloading. The physical bases of the model (particle representation) correspond to compaction, and early and intermediate stages of sintering. It has been, however, shown here that the mathematical description can also be successfully applied to the late stage sintering.

In order to avoid complex scaling of the interaction laws the particle size and size distribution are the same as in the real powder. Due to the computational limitation the size of the powder specimen is scaled down assuming that it represents correctly the average material behavior in the real specimen. This assumption is justified if the real specimen can be considered as uniform.

Consequently, an uniform temperature distribution is assumed in the discrete element specimen and the heat conduction is neglected. The temperature evolution is prescribed in agreement with that in the real process. These assumptions are justified since the temperature changes in the hot pressing process are very slow.

The hot pressing model implemented in the DEM is a combination of the cohesionless contact model with friction (the Kelvin-Voigt system) for the initial powder compaction, heating (before sintering) and cooling (after sintering), and the viscoelastic model of sintering (the Maxwell system) with the addition of thermal element related to the effect of thermal expansion. The first stage of a process of hot pressing is powder compaction, where a green body of a particulate material is formed. Powder compaction is modeled using the cohesionless contact model together with friction and an effect of thermal expansion (Fig. 6). The formulation of initial compaction model has considered only the elastic deformation of particles. Presented analysis concerns the relatively low values of external pressure and the hard and brittle NiAl material, thus the

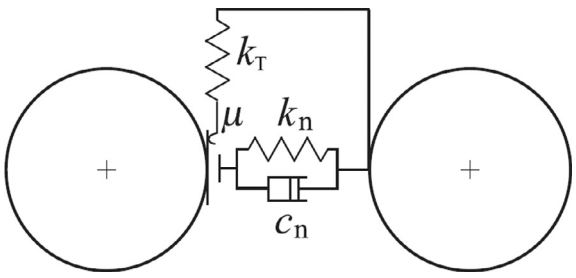

Fig. 6. Rheological scheme of the contact interaction for powder compaction.

contribution of elastic deformation in the total one is a predominant. This effect has been studied in [23].

The normal contact interaction is represented by the Kelvin-Voigt element consisting of a spring and a dashpot connected in parallel. Additionally, a thermal element is added in series with a spring. The normal contact force F_n is a sum of the elastic force in the spring F_n^e and the viscous component F_n^d

$$F_n = F_n^e + F_n^d. \tag{1}$$

The elastic part of the normal contact force F_n^e can be evaluated assuming the Hertz interaction model, which is the most classical nonlinear model used in particle collisions [24]:

$$F_n^e = \frac{2}{3}\left(\frac{E}{1-\nu^2}\right)\sqrt{\bar{r}}u_{rn}^{e\,\frac{3}{2}} \tag{2}$$

where E is the Young's modulus, ν is the Poisson's ratio and u_{rn}^e is the penetration of the two particles, calculated as

$$u_{rn}^e = d_{ij} - r_i(T) - r_j(T) \tag{3}$$

where d_{ij} is the distance of the particle centres, and $r_i(T)$, $r_j(T)$ their radii dependent on the temperature, and given by the following relation:

$$r_a(T) = r_a^0(1+\alpha\Delta T), \quad a = i,j, \tag{4}$$

where α is the linear coefficient of the thermal expansion, ΔT is the temperature increment, and r_a^0 $(a = i,j)$ is the a-the particle radius at the initial (reference) temperature.

The effective radius of particle $\bar{r}$, which allows to consider two particles with various radii, can be expressed as

$$\bar{r} = \frac{2r_i(T)r_j(T)}{r_i(T)+r_j(T)} \tag{5}$$

The viscous component of the normal force is assumed to be a linear function of the normal relative velocity v_{rn}

$$F_n^d = c_n v_{rn} \tag{6}$$

where

$$v_{rn} = (\dot{\mathbf{u}}_j - \dot{\mathbf{u}}_i)\cdot\mathbf{n}_i. \tag{7}$$

The value of the viscosity coefficient c_n can be taken as a fraction ξ of the critical damping C_{cr} for the system of two rigid bodies.

In the model of compaction no cohesion is allowed, so no tensile normal contact forces are allowed

$$F_n^e \leqslant 0. \tag{8}$$

The tangential reaction $\mathbf{F}_T$ at the contact point is brought about by the friction opposing the relative motion. The regularized Coulomb friction model has been assumed in the current model instead of the standard Coulomb law, which due to possible changes of the direction of sliding velocity would produce non physical oscillations of the friction force. The relationship between the friction force $\|\mathbf{F}_T\|$ and relative tangential u_{rT} displacement for the regularized Coulomb model (for a constant normal force F_n) is shown in Fig. 7.

The transition between the Kelvin-Voigt and Maxwell models has been characterized by an algorithm ensuring a smooth and numerically stable change. The detailed description of transition algorithm has been presented in [21]. The model transition time is strictly related to the temperature of sintering activation, which indicates an initiation of diffusional mechanism of mass transport. After reaching the temperature of sintering activation, the sintering model is performed.

Sintering stage has been modeled with an viscoelastic model (Fig. 8), which was developed on the basis of well-known viscous

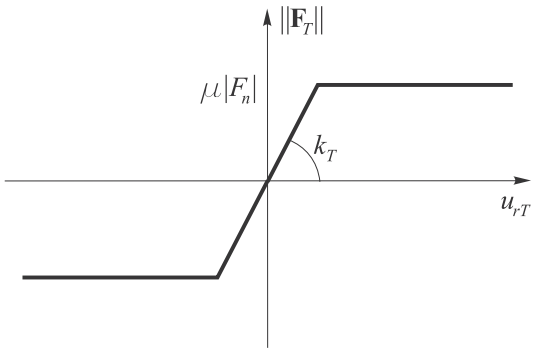

Fig. 7. Friction force vs. relative tangential displacement for the regularized Coulomb friction model.

model of sintering commonly used in the literature. Additionally, presented model takes into account the change of particle dimensions related to the effect of the thermal expansion.

The model of particle interaction during sintering takes into account cohesion between particles of a sintered material. Following Martin [10], the particle interaction during sintering is given by the equation derived considering mass transport and stresses at the grain boundary between two sintered particles:

$$F_n = \frac{\pi a^4}{8D_{\text{eff}}}v_{rn} + \pi\gamma_S\left[4r\left(1-\cos\frac{\Psi}{2}\right) + a\sin\frac{\Psi}{2}\right] \tag{9}$$

where F_n is the normal force between two particles, v_{rn} – the normal relative velocity, r – the particle radius, a – the radius of the interparticle boundary, Ψ – the dihedral angle, γ_S – the surface energy and D_{eff} – the effective grain boundary diffusion coefficient. The geometrical parameters of the model are defined in Fig. 9.

In the model of sintering, the initial particle boundary radius a_0 depends on the initial penetration u_{rn}^0, for instance induced by the compaction. From simple geometrical considerations we have

$$a_0 = \sqrt{\frac{ru_{rn}}{2}} \tag{10}$$

The growth of the radius of the interparticle boundary is governed by the following evolution law:

$$\dot{a} = -\frac{rv_{rn}}{a} \tag{11}$$

The particle boundary radius a grows until the sintering process is stopped. Its maximum at the equilibrium state is given by the following geometric relationship:

$$a_{\max} = r\sin\frac{\Psi}{2} \tag{12}$$

The model described by Eq. (9) has been derived for identical particles. Following Martin [10] it can be generalized to sintering models of different size particles by replacing the radius r in Eqs. (9)–(12) with the equivalent particle radius $\bar{r}$ given by the Eq. (5).

For the Maxwell element we have the following relationships for forces and velocities:

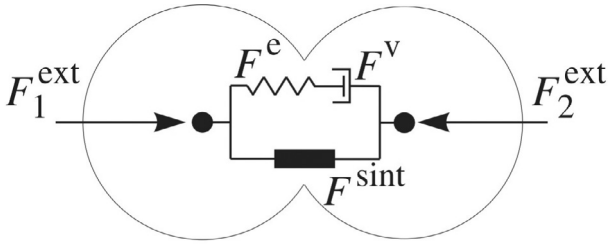

Fig. 8. Rheological scheme of the viscoelastic model of sintering under pressure.

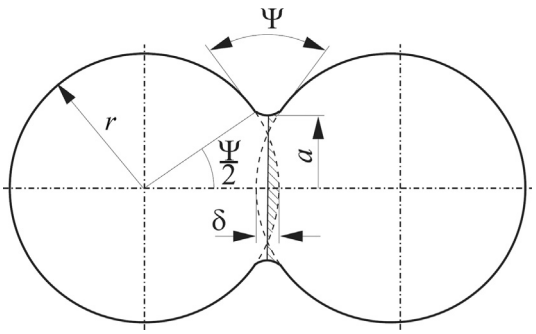

Fig. 9. Two-particle model of sintering.

$$F_n^v = F_n^e \tag{13}$$

$$v_{rn} = v_{rn}^v + v_{rn}^e \tag{14}$$

The viscous force is given by following form:

$$F_n^v = \eta v_{rn}^v \tag{15}$$

where

$$\eta = \frac{\pi a^4}{8 D_{eff}} \tag{16}$$

where D_{eff} is the effective grain boundary diffusion coefficient.

The elastic interaction of the normal contact force F_n^e has been presented in the form of the Hertz relationship analogously as in the initial compaction model (Eq. (2)). The rotational motion of the particles and tangential interaction has been neglected in the present formulation of sintering.

4. Determination of the material parameters of the sintering model

In the presented section the literatural studies of material parameters of viscoelastic model of sintering were performed. Relations to estimate the values of all required material model parameters were proposed. The analysis concerns the determination of diffusive parameters, as the main mass transport mechanisms of the sintering process assumed for the current model, and surface energy as the sintering driving force of particle attraction.

4.1. Diffusive parameters

The values of diffusive parameters directly depend on certain diffusion mechanism, which is considered at the constitutive model of sintering. In the presented work, the constitutive model of sintering was obtained from the analysis of the mechanism of the grain boundary diffusion, where the effective grain boundary diffusion coefficient D_{eff} is given by the following formula:

$$D_{eff} = \frac{D_{gb}\delta\Omega}{k_B T} \tag{17}$$

where D_{gb} is the grain boundary diffusion coefficient with the width δ, Ω is the atomic volume, k_B is the Boltzmann constant and T is the temperature.

The atomic volume Ω is a parameter indicating a volume of one gram of a material in normal conditions. The parameter is obtained from the quotient of the atomic mass m_a and theoretical density of a material ρ_{theo}:

$$\Omega = \frac{m_a}{\rho_{theo}} \tag{18}$$

The major diffusive parameter determining the kinetics of sintering process is the grain boundary diffusion coefficient D_{gb} given by the Arrhenius-type equation:

$$D_{gb} = D_{0gb} \exp\left[-\frac{\Delta H_{gb}}{RT}\right] \tag{19}$$

where D_{0gb} is the pre-exponential factor of grain boundary diffusion, ΔH_{gb} is the activation enthalpy of grain boundary diffusion, R is the gas constant.

The pre-exponential factor D_{0gb} is not very much different from those of lattice diffusion D_0, which is expressed as:

$$D_0 = D_0' \exp\frac{\Delta S}{R} \tag{20}$$

where ΔS is the diffusion entropy (ranges from 1 to several R) and D_0' contains geometric factors, the correlation factor, the lattice parameter squared, and an attempt frequency of the order of the Debye frequency. The form of pre-exponential factor D_0' depends on the diffusion mechanism. During the sintering process, atoms change their location via the vacancy mechanism of self-diffusion, which is the most basic diffusion process for grain boundaries. The pre-exponential factor D_0' in self-diffusion takes form [25]:

$$D_0' = f v_D \lambda^2 \tag{21}$$

To calculate the parameter D_0', the following parameters have to be determined:

- The Debye frequency v_D is a theoretical maximum frequency of vibration for the atoms that make up the crystal. The Debye frequency in solids usually ranges between $10^{13} - 10^{14}$ Hz and it can be determined from Eq. (22):

$$v_D = v_s \left[\frac{3N_a}{4\Pi V_u}\right]^{1/3} \tag{22}$$

  where v_s is the speed of sound, N_a is the number of atoms in the unit cell and V_u is the volume of unit cell.
- Lattice parameter λ is given by various formula for different types of crystal system. For the most two popular crystal systems: face-centered cubic FCC (for example cooper – Cu) and body-centered cubic BCC (intermetallic NiAl), lattice parameters depend on an atomic radius r_{at}, and can be calculated from the following formulas:

  FCC - $\lambda_{Cu} = \frac{4r_{at}}{\sqrt{2}}$.

  BCC - $\lambda_{NiAl} = \frac{4r_{at}}{\sqrt{3}}$.
- Correlation factor f depends on the crystal unit cell. For monovacancies in cubic lattices f is a temperature-independent quantity, which is approximately given by:

$$f \approx 1 - \frac{2}{Z} \tag{23}$$

  where Z is the coordination number. Exact values of correlation factor f are listed in Table 2.

Finally, comparing Eqs. (19)–(21), we obtain the relation of grain boundary diffusion coefficient D_{gb} with its all component:

$$D_{gb} = f v_D \lambda^2 \exp\left[\frac{\Delta S}{R}\right] \exp\left[-\frac{\Delta H_{gb}}{RT}\right] \tag{24}$$

The enthalpy of activation ΔH_{gb} appearing in Eq. (24) is defined as a minimum energy needed to create or change the thermodynamic system. It plays a major role in the diffusivity characterization, which is closely related to the type of diffusion. Following Mehrer [26], the relation between the enthalpy of activation of

Table 2
Correlation factors of vacancy-mediated self-diffusion in cubic lattices [25].

Structure	fcc	bcc	sc	diamond
f	0.7815	0.727	0.653	0.5

bulk diffusion ΔH, grain boundary diffusion ΔH_{gb} and surface diffusion ΔH_s and their equivalent diffusion coefficients can be stated as follows:

$$\Delta H > \Delta H_{gb} > \Delta H_s \tag{25}$$

$$D \leqslant D_{gb} \leqslant D_s \tag{26}$$

Coefficients of grain boundary diffusion ($D_{gb}, \Delta H_{gb}$) lie between those for bulk diffusion (high enthalpy of activation ΔH, low diffusivity D) and surface diffusion (low enthalpy of activation ΔH_s, high diffusivity D_s). Typically, grain boundary diffusion in metals is four to six orders of magnitude faster than bulk diffusion. For metals, the ratios of activation enthalpies of bulk and grain boundary self-diffusion, $\Delta H_{gb}/\Delta H$, lie between 0.4 and 0.6. Studies refering to empirical correlations between grain boundary self-diffusion properties for different crystal systems were derived either in [27,28] (Table 3).

The grain boundary width δ taken to the presented considerations with the value of 0.5 nm, suggested by Fisher [29], proved to be a good assumption. The following value is consistent with the determinations of δ by a high-resolution electron microscopy and other techniques [30].

4.2. Surface energy and dihedral angle

One of the major driving forces for densification during sintering is the change in free energy from the decrease in surface area and lowering of the surface free energy by the replacement of solid-vapour interfaces [31]. The forces must balance at the junction where the surfaces of the pores meet the particle boundary (Fig. 10). They are normally represented by the tension in the interface, i.e., the tension in the solid–vapor interface γ_s (surface energy) and the tension in the grain boundary γ_{gb} (grain boundary energy). At the junction the tension in the solid–vapor interface is tangential to that interface, while that in the grain boundary is in the plane of the boundary [32]. The balance of forces leads to

$$\gamma_{gb} = 2\gamma_s \cos\frac{\Psi}{2} \tag{27}$$

where Ψ is the dihedral angle.

The dihedral angle can be determined only by interfacial energies and is independent of the pressures in the phases. This means that the dihedral angle is constant, irrespectively of the pressure of the vapour phase, where Ψ is larger than 120°, because γ_s is usually higher than γ_{gb}. In general, γ_s is 2–3 times higher than γ_{gb} and Ψ is around 150° [33].

To determine the value of dihedral angle of the specific material, the surface γ_s and grain boundary energy γ_{gb} should be calculated. It should be noticed that the estimation of surface and grain boundary energies can be held for the single particle, thus the final result of the study of surface energy of policrystalline material will be a statistic representation of these parameters.

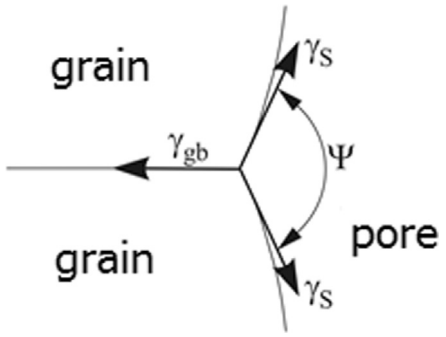

Fig. 10. The equilibrium state of the pores in polycrystalline solids with the balance of the surface and grain boundary energy.

Generally, the determination of the surface energy is performed via the experimental measurements [34], however there are several models concerning calculations of the surface energy of metals either from first-principles (density functional theory) [35] or by semi-empirical methods [36]. Despite serious difficulties and the complexity of many techniques and models, the surface energy can be estimated by at fairly simple relation proposed by Kislyi and Kuzenkova [37], which is based on the Herring's relation [38]:

$$\gamma_s \geqslant \frac{Gb}{4\pi(1-\nu)} \tag{28}$$

where G is the shear modulus, b the Burgers vector and ν the Poisson's ratio.

The second parameter needed to be calculated is the grain boundary energy γ_{gb}. It is dominated by the combination of surface energies due to the force balance on the junction of particles. The grain boundary energy results from mismatch between atoms across the boundary. Similarly to the surface energy, the grain boundary energy is hard to calculate and generally it can be determined via the experimental, numerical and analytical approaches. The experimental measurements of γ_{gb} are performed using similar techniques as γ_s. The measurement of dihedral angles at triple lines is the most useful and popular method, however in the literature more sophisticated approaches can be found [39]. Theoretical values of grain boundary energy can be computed by the numerical modeling using molecular statics or molecular dynamics [40]. The analytical description of grain boundary energy depends on the type of grain boundary – low or high angle. Although the structure of the low angle grain boundaries is reasonably well understood, much less is known about the structure of the high angle grain boundaries, which are dominant in the policrystalline assembly [41]. Based on the literture studies it can be stated that the typical values of grain boundary energies of metals vary from 0.32 J m^{-2} for Al to 0.87 for Ni J m^{-2} [42].

Table 3
Empirical correlation between grain boundary self-diffusion for different crystal systems, and the melting temperature T_m [27,28]. For the grain boundary width the value of δ = 0.5 nm was assumed.

Structure	Brown (1963)		Gust et al. (1985)	
	D_{0gb} [m^2 s^{-1}]	ΔH_{gb} [J mol^{-1}]	D_{0gb} [m^2 s^{-1}]	ΔH_{gb} [J mol^{-1}]
fcc	$1.89 \cdot 10^{-5}$	$83.0 \cdot T_t$ [K]	$1.94 \cdot 10^{-5}$	$74.4 \cdot T_t$ [K]
bcc	$0.67 \cdot 10^{-3}$	$97.6 \cdot T_t$ [K]	$1.84 \cdot 10^{-5}$	$86.7 \cdot T_t$ [K]
hcp	$0.55 \cdot 10^{-4}$	$89.8 \cdot T_t$ [K]	$1.94 \cdot 10^{-5}$	$85.4 \cdot T_t$ [K]

5. Numerical simulation of hot pressing process

Numerical studies involve the simulations of the hot pressing process of intermetallic NiAl material which was studied through the experiment in Section 2. This section considers the generation of the geometrical model of powder specimen, the calibration and validation of the hot pressing model through numerical simulations. Simulations will be performed using a cylindrical specimen smaller than the real one but in keeping with the real size and the size distribution of powder particles.

5.1. Generation of the geometrical model of powder specimen

The purpose of presented subsection is the generation of the discrete element geometrical model of powder specimen satisfying the main requirements, such as the material isotropy, irregular configuration of particles, the real particle size distributions, relatively low porosity and a dense packing of powder particles. Discrete element specimen with prescribed size distribution filling the cylindrical container have been generated using a specially developed original numerical algorithm. The generation algorithm consists of two stages. Firstly, a set of loose particles with a given size distribution randomly distributed in space cells is generated (Fig. 11a). Next, the particles are compacted using a dynamic method (under the gravity and prescribed contraction of the boundary surfaces) to achieve a densely packed specimen. Using this procedure two specimens have been generated:

- the smaller specimen with diameter 0.058 mm and height 0.095 mm (Fig. 11b) consisting of 1751 particles of diameters ranging from 1.5 to 19.5 μm,
- the larger specimen with diameter 0.125 mm and height 0.182 mm (Fig. 11c) consisting of 17510 particles of diameters ranging from 1.5 to 19.5 μm,

The larger specimen has been generated in order to verify the results obtained with the smaller specimen, which is computationally less costly.

The particles have been generated using the real particle size distribution shown in Fig. 3b. Due to a small size of the numerical specimens, the biggest particles of the intermetallic powder ($d_p > 20$ μm) were not considered in the numerical models. The particle size distribution in the discrete element models according to the number and volume of particles is presented in Fig. 12a and b, respectively. The numerical distribution according to the number in Fig. 12a is compared with the experimental distribution, showing a good coincidence.

The generated specimens should represent correctly initial conditions of powder materials before the hot pressing process. The porosity or, equivalently, the relative density defined as the ratio of the bulk density and the theoretical density of non-porous material, are the main parameters characterizing a granular material. The two generated specimens have the relative density of 0.665 (the smaller specimen) and 0.686 (the larger one). The process of the specimen generation is characterized by a certain randomness, therefore the results obtained for the two specimens are slightly different. This, however, corresponds to the random character of the real process. A scatter has also been observed in the relative density measurements in the laboratory. The relative poured density of the NiAl powder varied from 0.625 to 0.680 [23]. As it can be seen the relative density of the two generated specimens agrees well with experimental results.

5.2. Calibration of the hot pressing model

The specimen of intermetallic NiAl generated in the previous section, have been used in simulation of the whole manufacturing process. The present section shows calibration of the model. Preliminary values of the material model parameters have been determined based on the data from the literature. Then, the parameters have been tuned by adjustment of the numerical density evolution to the experimental data for a selected case of laboratory tests described in Section 2.

The particle interaction model is defined by the diffusion parameters (the atomic volume Ω and the pre-exponential factor of the grain boundary diffusion D_{0gb}), the elastic constants (Young's modulus E and Poisson's ratio ν) and the parameters resulting from surface tension (surface energy γ_s and dihedral angle Ψ). The material parameters of sintering model were estimated on the basis of equations and relations presented in the Section 4 and confronted with the literature data [43–45]. Procedure of the evaluation of material model parameters of NiAl material has been presented in Appendix. The material data of intermetallic powder used in the calibration process has been shown in Table 4.

In the calibration procedure, the activation enthalpy of grain boundary diffusion, ΔH_{gb}, has been treated as a fitting parameter. The obtained value of ΔH_{gb} of intermetallic material is in correspondence with experimental measurements [46] and the empirical approximation for BCC materials (NiAl) [27]. Table 4 contains the final value of the parameter ΔH_{gb} obtained in the calibration.

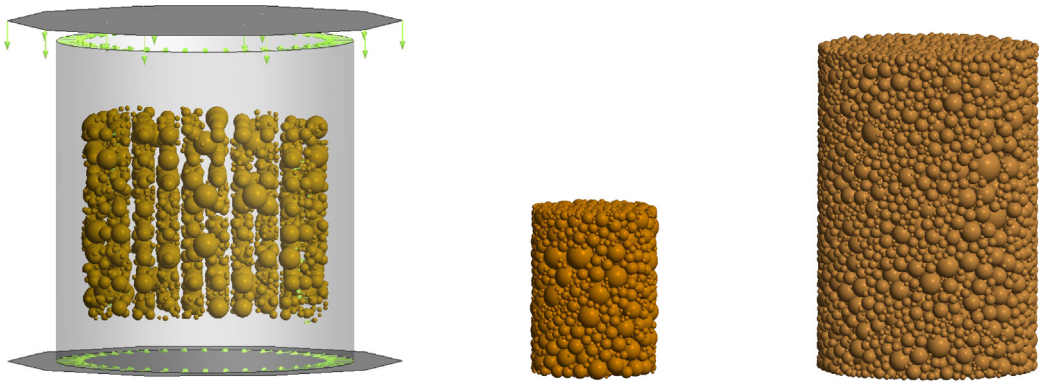

Fig. 11. Generation of the geometrical model: (a) scheme of the compaction of the loosely-packed discrete elements based on the dynamic methods, (b) the smaller specimen (1751 particles), (c) the larger specimen (17,510 particles).

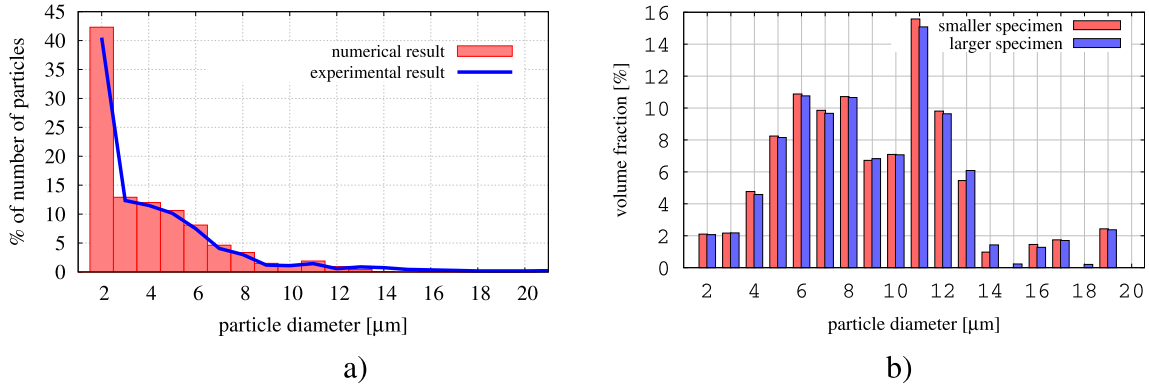

Fig. 12. Particle size distribution in the discrete element models: (a) number distribution (small specimen), (b) volume distribution (both smaller and larger specimen).

The numerical model for NiAl powder has been calibrated for the external pressure $p = 30$ MPa, sintering temperature $T_s = 1400$ °C (1673 K) and sintering time $t_s = 30$ min. The temperature and pressure profiles of the whole process are presented in Fig. 13.

Temperature was increased with the heating rate of 15 °C/min. Beginning of sintering for NiAl powder has been assumed at temperature of 683 °C. Following Lis and Pampuch [47], the temperature corresponding to 0.5 of the melting point have been taken assuming as an appropriate temperature of grain boundary diffusion activation. Specimen was kept at the sintering temperature, $T_s = 1400$ °C, during the sintering time, $t_s = 30$ mins, and cooled to the room temperature with the cooling rate of 10 °C/min. In order to increase numerical efficiency, the mass of intermetallic particles has been algorithmically scaled by factors 10^{17} in a similar way as in [21].

The configurations of the NiAl specimen before and after sintering are shown in Fig. 14. The shrinkage of the specimen during sintering can be clearly noticed.

Volume changes of the NiAl specimen during the whole process are presented in Fig. 15. Except for the volume changes represented by the volumetric shrinkage ϕ_V, Fig. 15 presents the evolution of the linear shrinkage in x, y and z direction, denoted by ϕ_x, ϕ_y, ϕ_z. The shrinkage parameters has been calculated from the following relationships:

$$\phi_x = \frac{R_x}{R_{0x}}, \quad \phi_y = \frac{R_y}{R_{0y}}, \quad \phi_z = \frac{H}{H_0}, \quad \phi_V = \frac{V}{V_0} \tag{29}$$

where R_x and R_y are the bulk radii of the geometrical model of the specimen in the x and y direction, R_{0x} and R_{0y} are the initial radii of geometrical model, H and H_0 are the bulk and initial height of the geometrical model, respectively, and V and V_0 are the bulk and initial volume, respectively.

Table 4
Material parameter data of NiAl powder.

Material constant	Parameter value
Mean atomic volume, Ω [m^3]	$1.20 \cdot 10^{-29}$
Pre-exponential factor of the grain-boundary diffusion, D_{0gb} [m^2/s]	$2.55 \cdot 10^{-5}$
Activation enthalpy of grain-boundary diffusion, ΔH_{gb} [kJ/mol]	184
Grain-boundary width, δ [nm]	0.5
Young's modulus, E [GPa]	183
Poisson's ratio, ν	0.34
Surface energy, γ_s [J/m^2]	1.57
Dihedral angle, Ψ [°]	145
Density, ρ_{theo} [kg/m^3]	5910
Coefficient of thermal expansion, α [10^{-6} K^{-1}]	11.5

The shrinkage of the specimen leads to the increase of the density. The relative density for the whole process was determined using the following equation:

$$\rho_{rel} = \frac{\rho}{\rho_{theo}} \tag{30}$$

where ρ is the bulk density, ρ_{theo} is the temperature-dependent theoretical density given by equation:

$$\rho_{theo} = \frac{\rho^0_{theo}}{(1 + \alpha \Delta T)^3} \tag{31}$$

where ρ^0_{theo} is the theoretical density at the room-temperature, α is the linear coefficient of the thermal expansion and ΔT is the temperature increment. The bulk density ρ has been determined taking the powder mass and the specimen volume at the considered time.

The numerical model of powder metallurgy has been calibrated using the results of laboratory tests of sintering of NiAl in condition of $T_s = 1400$ °C and $p = 30$ MPa, presented in the Table 1 in Section 2. The numerical curve showing evolution of the relative density of NiAl material obtained as a result of the calibration procedure are compared with experimental in Fig. 16. It can be seen that the numerical curves (for both cases – the smaller and larger specimen) represent quite well density changes in the real process. Comparing the density evolution from two DEM specimens it can be seen that the results are quite similar (especially at the sintering stage). A small difference at the beginning of the process results from the higher poured density of the larger specimen. This difference is reduced during the compaction stage due to the particle rearrangement and finally, the two curves practically coincide at the sintering stage. This shows that the smaller specimen is representative for simulation of the process and it will be used further on in the numerical studies.

Fig. 16 shows the process stages and the models applied in the analysis of these stages. The curve in Fig. 16 allows to analyze densification mechanisms during the process. Initially it can be observed a certain increase of relative density under the applied punch loading. During the heating the relative density does not change. When the material is heated the volume of the specimen grows as it can be observed in Fig. 15, but at the same time the theoretical density increases proportionally so the relative density remains unchanged. After reaching the temperature of sintering activation, densification begins. In the initial stage of sintering the growth of densification is relatively low, because the diffusion processes are limited at low temperature. Fig. 17 presents the evolution of the diffusion coefficient D_{gb} of NiAl material as the functions of temperature. The value of D_{gb} increases with temperature

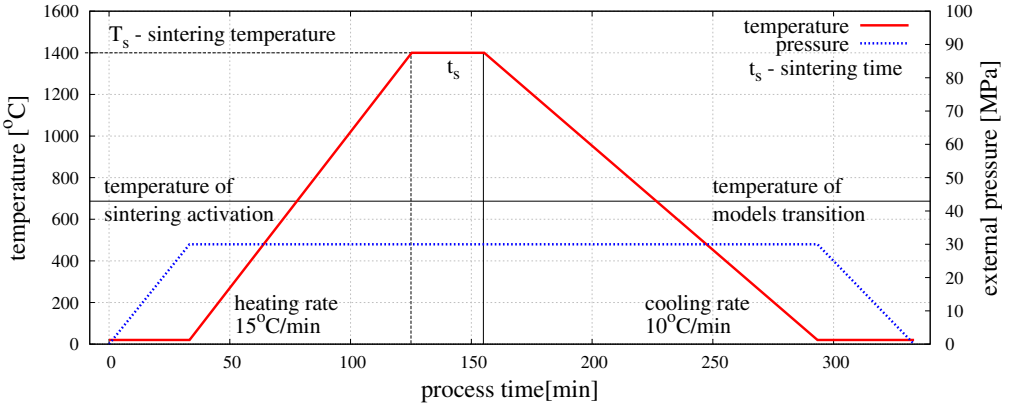

Fig. 13. Temperature and pressure profiles for the powder metallurgy process of intermetallic powder at $T_s = 1400\,^{\circ}\mathrm{C}$, $t_s = 30$ mins and $p = 30$ MPa.

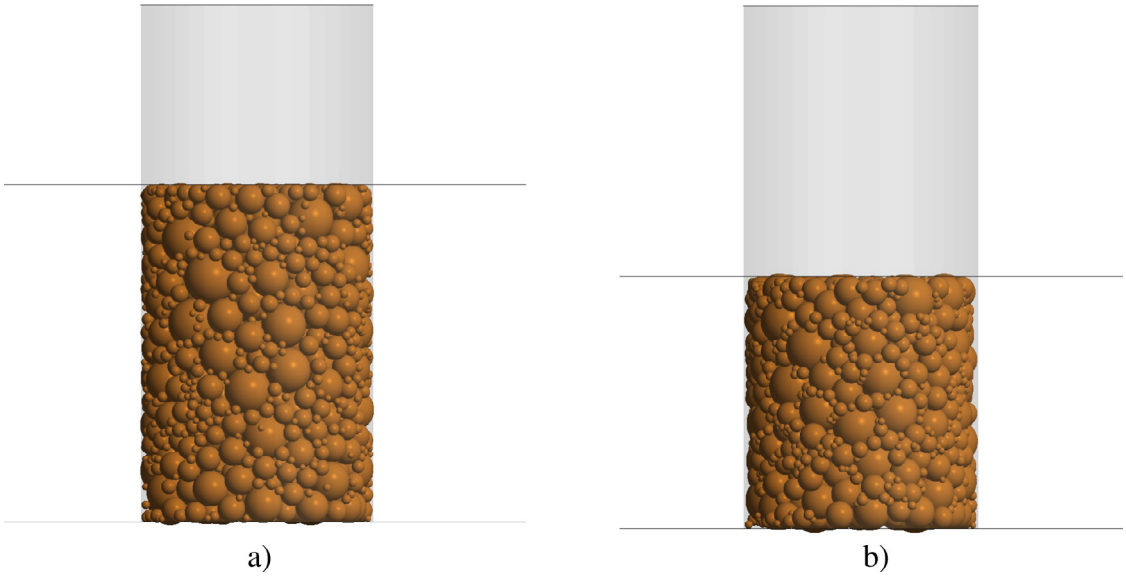

Fig. 14. The geometrical model of NiAl specimen: (a) before sintering, (b) after sintering.

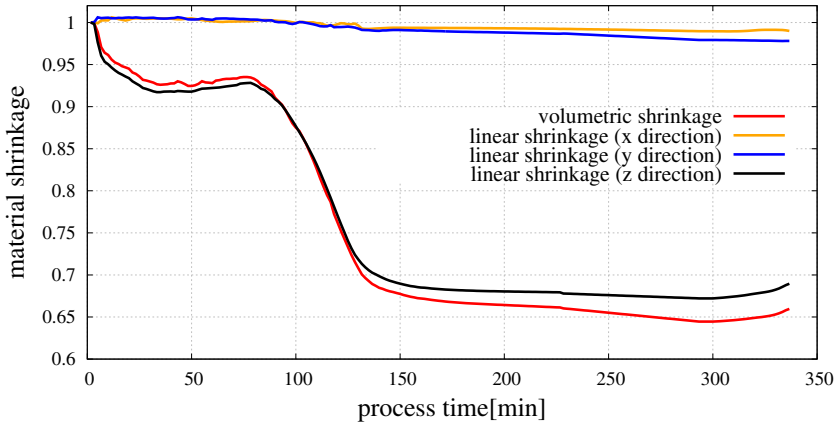

Fig. 15. Evolution of the volumetric and linear shrinkage of the intermetallic specimen (the smaller one).

and furthermore lowers the viscosity of particle, which favors the densification. Simultaneously, the growth of temperature reduces the material stiffness, which is favorable for particles penetration and rearrangement. The evolution of the Young's modulus of NiAl material as the functions of temperature taken from [48] and presented in Fig. 17 has been implemented in the numerical algorithm.

As the temperature increases, the growth of densification accelerates. This particular effect can be seen in Fig. 18, where the dependence of the densification rate and relative density has been

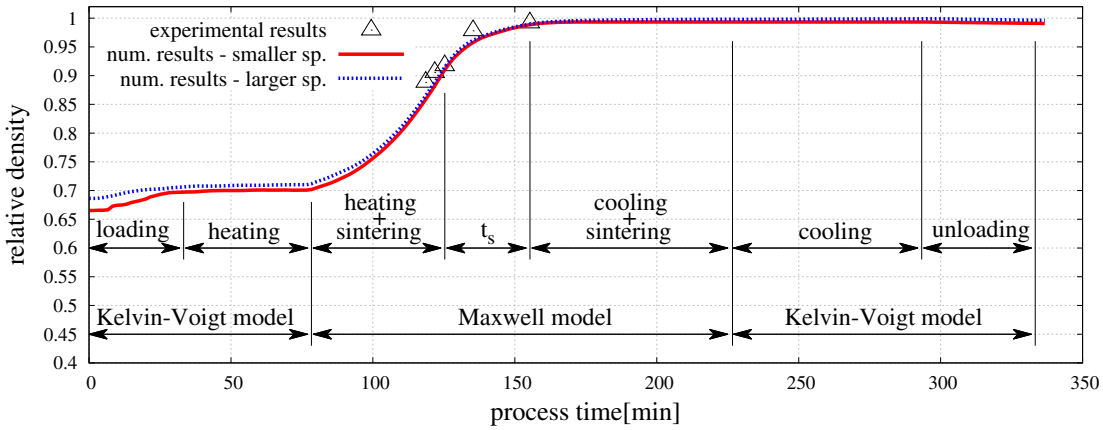

Fig. 16. Evolution of the relative density of NiAl powder during the whole process.

shown. Densification rate $\dot{\rho}_{rel}$ has been treated as the increment of relative density $\Delta\rho_{rel}$ in certain increment of time Δt:

$$\dot{\rho}_{rel} = \frac{d\rho_{rel}}{dt} = \frac{\Delta\rho_{rel}}{\Delta t} \tag{32}$$

It can be seen in Fig. 18 that from the value of relative density corresponding to the transition of models and activation of sintering ($\rho_{rel} = 0.705$ - NiAl) the materials densification increases with a near linear rate, which is typical for the intermediate stage of sintering. The highest densification rate can be seen near the value 0.90 of the relative density, while the sintering temperature $T_s = 1400\,^{\circ}C$ is achieved. In this particular moment the viscosity and stiffness of discrete elements are at their lowest levels. After this point, during the sintering time $t_s = 30$ min, the material is compacted with a constantly decreasing rate. This can be seen in Figs. 16 and 15, where the relative density and the volumetric shrinkage are gradually stabilized. This effect is characteristic for the final stage of sintering - the penetration of particles is blocked by a high viscosity of material. The value of η calculated according to Eq. (16) rises because of the increase of the neck radius, which results in a higher value of the viscous resistance. Furthermore, the neck radius a of most particle connections reaches the maximum value at the equilibrium state a_{max} (given by Eq. (12)), which signifies the end of sintering. At this point, the relative density of considered material reaches values very close to 1 ($\rho_{rel} = 0.993$), which means that an almost fully dense material has been obtained. As the material is cooled, the relative density may slightly increase due the impact of mass transport mechanism of particles, which have not achieved the equilibrium state yet. After reach the temperature of sintering activation/deactivation the relative density is constant, even though the dimensions and volume of the material decrease due to the thermal expansion effect. All the changes of the specimen volume and material density obtained in the analysis agree very well with the changes observed in a real process.

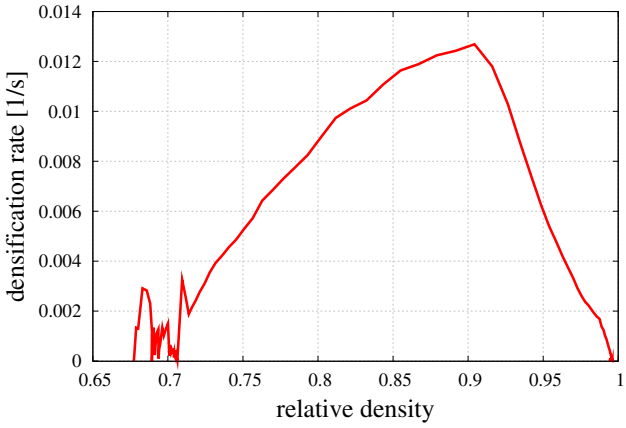

Fig. 18. Dependence of the densification rate in the function of relative density.

5.3. Validation of hot pressing model at different process parameters

The material model parameters given in Table 4 determined in the calibration procedures in the previous sections for one set of process parameters (process No. I) have been employed in

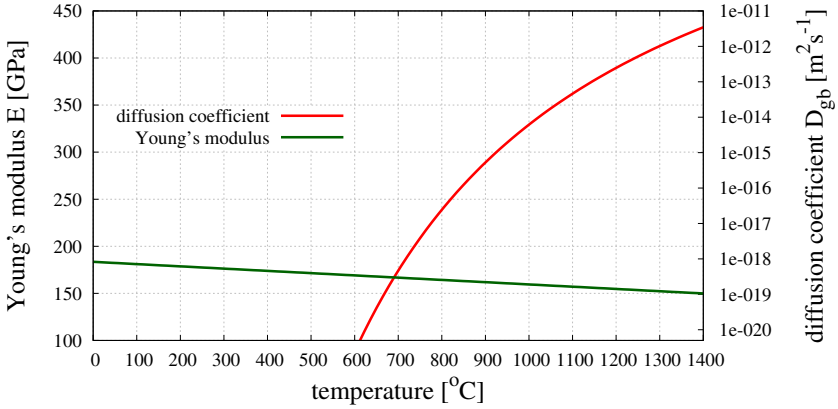

Fig. 17. Evolution of the Young's modulus and diffusion coefficient of NiAl material in the function of temperature.

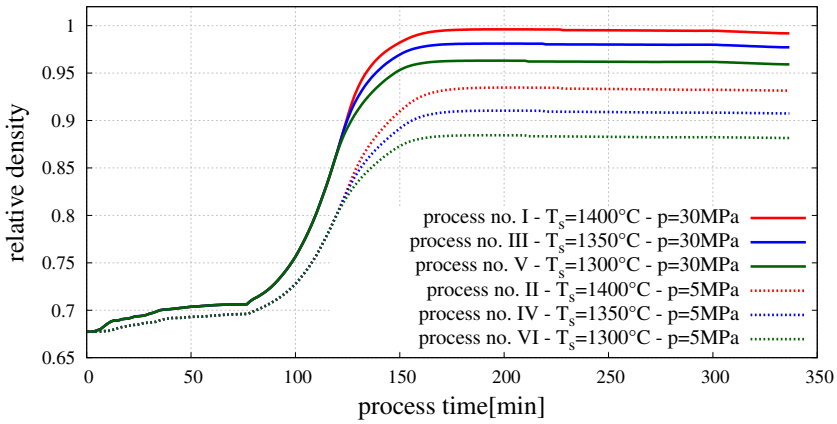

Fig. 19. Evolution of the relative density of the intermetallic material for different sintering process parameters.

simulation of hot pressing processes with different combinations of parameters (sintering temperature T_s, external pressure p) defined in Table 1. The sintering time was the same for all the analyses ($t_s = 30$ mins).

The purpose of this section has been to validate the numerical model by comparing numerical and experimental results for different sets of sintering process parameters. Furthermore, the influence of applied process parameters on the sintering kinetics has been studied. Numerical simulations have employed the same geometrical model of the initial dense specimens as in the calibration.

Evolution of the relative density for the NiAl powders for all the processes is presented in Fig. 19. The results show the correct performance of the numerical model. Comparison of the plots corresponding to a different pressure and the same temperature allows to assess an influence of the pressure. It can be seen, that generally, a higher external pressure gives a higher green density and faster and higher densification during sintering.

The curves in Fig. 19 allow to asses the influence of the sintering temperature T_s on the densification of the powder. An increase of densification for the higher sintering temperature, which is proper result of numerical simulations, can be seen. The temperature affects the diffusion parameters, the effective diffusion coefficient of the grain boundary D_{eff} and the diffusion coefficient for vacancy transport in the grain boundary D_{gb}, which are one of the major indicators of sintering kinetics. The higher sintering temperature is, the lower the viscosity of the material is, which results in a higher diffusion rate and easier particle penetration. Influence of sintering temperature T_s on the NiAl material densification is smaller than that of the external pressure, especially in the case of the external pressure of 30 MPa, where the differences of the relative density after 30 min of sintering at temperature $T_s = 1300$ °C and 1400 °C are about 3%. In case of the specimens sintered at the pressure of 5 MPa at the same sintering temperature, differences are approximately 4%.

The relative density evolution obtained in the numerical simulation has been confronted with experimental measurements in Fig. 20. DE model has been validated by 18 density points in 6 combinations of sintering temperature and external pressure. The graph shows the sintering stage only, excluding the compaction and cooling stages. A reasonably good correspondence between the numerical results and experimental data can be observed in most cases. The curves representing the numerical results pass through or close to the experimental points.

6. Conclusions

This paper shows a numerical and experimental analysis of intermetallic NiAl material manufacturing with the use of the hot pressing technique. The paper presents the formulation and development of an original numerical model of hot pressing within the framework of the discrete element method. The presented model is an extension of the Authors' models presented in their earlier work with the addition of thermal element related to the effect of thermal expansion. In this research investigation the main stages of hot pressing - the initial powder compaction and pressure-assisted sintering - have been modelled together within the same simulation. For the purposes of numerical simulations the analysis of relations of material parameters of the sintering model has been carried out to estimate the values of all required parameters. The resulting appropriate material model parameters have been used in the simulations of hot pressing for different combinations of process parameters to calibrate and validate the numerical model based on the Authors' experimental results. Calibration has involved the adjustment of numerical results of density evolution to the experimental data. Numerical calibration has been performed in selected cases of the tests. The remaining experimental results have been used for the validation of the model. Numerical validation has shown the correct representation of density, shrinkage and densification rate of the sintered specimens for different combination of process parameters. The results also prove that the subject literature on material model parameters of the sintering model has been well reviewed and the further estimation of parameters values - well carried out.

Acknowledgments

The results presented in the paper have been obtained within the projects funded by the National Science Centre awarded by decision numbers DEC-2012/05/N/ST8/03376 and DEC-2013/11/B/ST8/03287.

Appendix A

The section presents the procedure of the estimation of sintering material parameters in the example of intermetallic NiAl material. The sintering material parameters were calculated on the basis of the equations and relations presented in the Section 4. To execute the simulation of the sintering process, the following material parameters must be evaluated:

- mean atomic volume Ω depends on the atomic mass m_a and density d and is given by Eq. (18). In the case of intermetallic NiAl, Eq. (18) is not completely satisfied by the presence of two types of atoms - Ni and Al. The value of the atomic volume of NiAl can be calculated by taking the mean value of the atomic mass of Ni and Al:

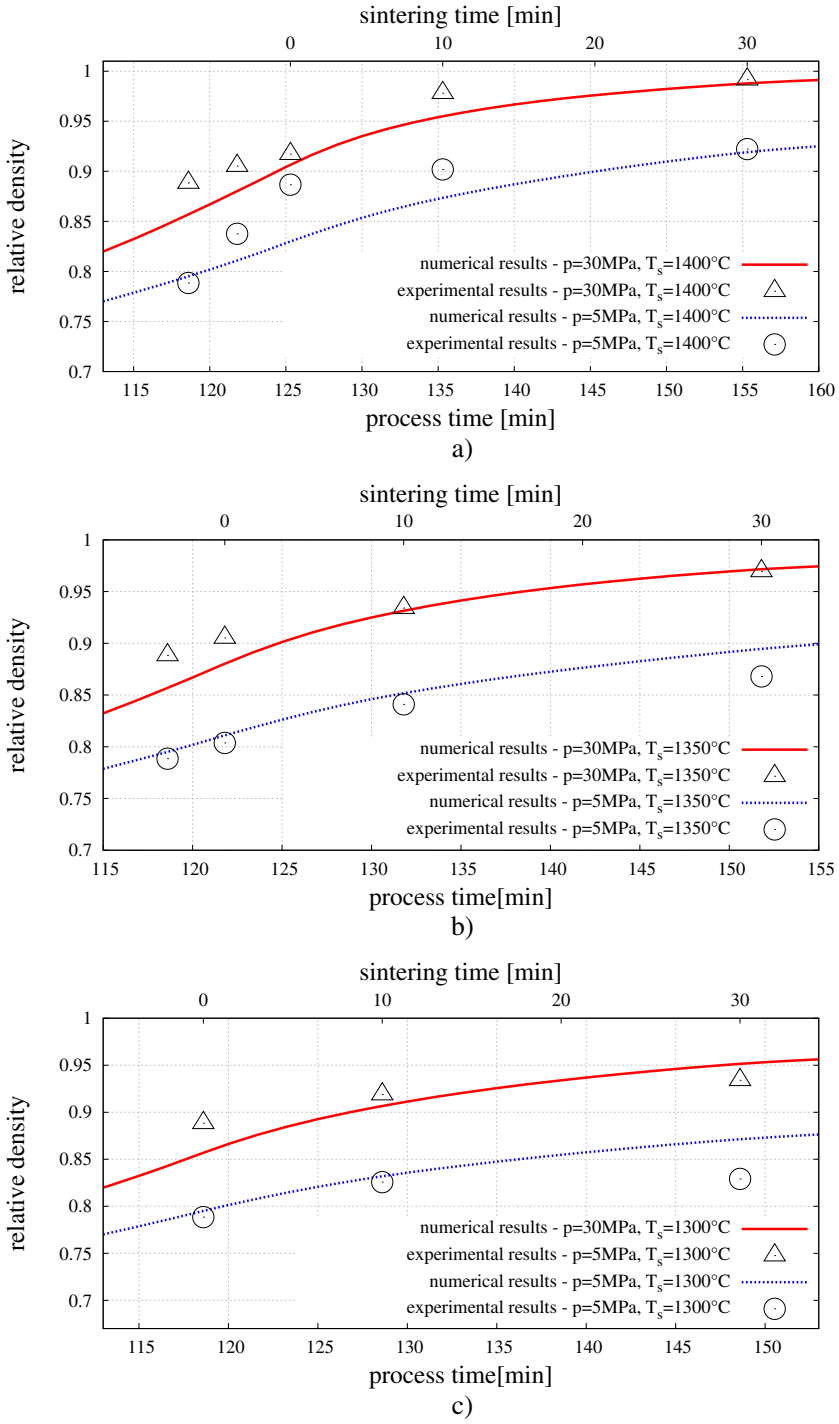

Fig. 20. Density evolution – numerical and experimental results of pure NiAl sintering with pressure 5 and 30 MPa and sintering temperature of: (a) $T_s = 1400\ ^\circ$C, (b) $T_s = 1350\ ^\circ$C, (c) $T_s = 1300\ ^\circ$C.

$m_a^{\mathrm{Ni}} = 58.69$ u,
$m_a^{\mathrm{Al}} = 26.98$ u,
$d^{\mathrm{NiAl}} = 5910\ \mathrm{kg/m^3}$.

Atomic mass m_a is expressed by u - *unified atomic mass units*, which is equal to $1.66 \cdot 10^{-27}$ kg, thus:

$$\Omega = \frac{m_a^{\mathrm{Ni}} + m_a^{\mathrm{Al}}}{2 \cdot d^{\mathrm{NiAl}}} = \frac{(58.69 + 26.98) \cdot 1.66 \cdot 10^{-27}\ \mathrm{kg}}{2 \cdot 5910\ \mathrm{kg/m^3}} = 1.20 \cdot 10^{-29}\ \mathrm{m^3}$$

- thickness of the grain-boundary δ has been taken from [29] as the value of $\delta = 0.5$ nm as to be a good estimation.
- the pre-exponential factor of grain-boundary diffusion $D_{0\mathrm{gb}}$ given by Eq. (20), can be estimated from the following calculation:

$$D_{0\mathrm{gb}} = D'_{0\mathrm{gb}} \exp\left(\frac{\Delta S}{R}\right) = 7.69 \cdot 10^{-7}\ \frac{\mathrm{m^2}}{\mathrm{s}} \exp\left(\frac{3.5\mathrm{R}}{\mathrm{R}}\right) = 2.55 \cdot 10^{-5}\ \mathrm{m^2/s}$$

where:
$\Delta S = 3.5R$ (taken from [25]),
$D'_{0gb} = 7.69 \cdot 10^{-7}$ m²/s, calculated from Eq. (21):

$$D'_{0gb} = f \nu_D \lambda^2 = 0.727 \cdot 1.27 \cdot 10^{13}\ \text{Hz} \cdot (2.887 \cdot 10^{-10}\ \text{m})^2 = 7.69 \cdot 10^{-7}\ \text{m}^2/\text{s}$$

where:
$f = 0.727$,
$\nu_D = 1.27 \cdot 10^{13}$ Hz (calculated from Eq. (22)),
$\lambda = 2.887 \cdot 10^{-10}$ m.

The obtained value of pre-exponential factor of grain-boundary diffusion of NiAl is in the good correspondence with the literature data [44], where D_0 parameter of the stoichiometric policrystalline NiAl varies between $2.71^{+10.0}_{-2.14} \cdot 10^{-5}$ and $2.77^{+2.25}_{-1.24} \cdot 10^{-5}$ m²/s.

- *Young's modulus E* is a temperature-depended parameter and in the sintering conditions (1400 °C) its value is lower (≈ 150 GPa [48]) than in the room-temperature (182 GPa).
- *Poisson's ratio ν*, analogically to Young's modulus, depends on the temperature conditions. The temperature dependence of Poisson's ratio for NiAl has been calculated from the Young's modulus and the shear modulus in [49]. Applying given consideration, ν in the sintering conditions of 1400 °C can be calculated by:

$$\nu = 0.307 + 2.15 \cdot 10^{-5} T = 0.307 + 2.15 \cdot 10^{-5} \cdot 1673 = 0.34$$

where T is the temperature in Kelvin.

- *Surface energy* γ_s depends on the materials constants, such as the shear modulus G, the Burgers vector b and the Poisson's ratio ν. The value of γ_s can be estimated by the fairly simple relation (Eq. (28)):

$$\gamma_s = \frac{Gb}{4\pi(1-\nu)} = \frac{(52\ \text{GPa} \cdot 2.5 \cdot 10^{-10}\ \text{m})}{(4\pi(1-0.34))} = 1.57\ \text{J/m}^2$$

where:
$G = 52$ GPa in temperature of 1400 °C,
$b = 2.5 \cdot 10^{-10}$ m (calculation based on [50]),
$\nu = 0.34$ in temperature of 1400 °C.

The surface energy value of intermetallic NiAl has been measured and simulated in [45], where the average energy for all studied surfaces of NiAl material was 1.53 J/m², thus the calculated value is relatively closed to with the literature data.

- *Dihedral angle* Ψ can be evaluated by the interfacial energies: the surface energy γ_s and the grain-boundary energy γ_{gb}, using the Eq. (27), which can be transformed to the following form:

$$\Psi = 2\arccos\left(\frac{\gamma_{gb}}{2\gamma_s}\right) = 2\arccos\left(\frac{0.94\ \text{J/m}^2}{2 \cdot 1.58\ \text{J/m}^2}\right) = 145^\circ,$$

where:
$\gamma_s = 1.57$ J/m² was calculated from Eq. (28),
$\gamma_{gb} = 0.94$ J/m² was taken from [45] as a reasonable value of the average grain-boundary energy for NiAl.

References

[1] S. Luding, Cohesive, frictional powders: contact models for tension, Gran. Mat. 10 (2008) 235–246.
[2] S.J. Antony, N.P. Kruyt, Role of interparticle friction and particle-scale elasticity in the shear-strength mechanism of three-dimensional granular media, Phys. Rev. E 79 (2009) 031308.
[3] A. Balakrishnan, P. Pizette, C.L. Martin, S.V. Joshi, B.P. Saha, Effect of particle size in aggregated and agglomerated ceramic powders, Acta Mater. 58 (2010) 802–812.
[4] C.L. Martin, D. Bouvard, S. Shima, Study of particle rearrangement during powder compaction by the Discrete Element Method, J. Mech. Phys. Solids 51 (2003) 667–693.
[5] M. Pasha, S. Dogbe, C. Hare, A. Hassanpour, M. Ghadiri, Effect of particle size in aggregated and agglomerated ceramic powders, Gran. Mat. 16 (2014) 151–162.
[6] B. Storåkers, S. Biwa, P.-L. Larsson, Similarity analysis of inelastic contact, Int. J. Solids Struct. 34 (1997) 3061–3083.
[7] B. Storåkers, N.A. Fleck, R.M. McMeeking, The viscoplastic compaction of composite powders, J. Mech. Phys. Solids 47 (1999) 785–815.
[8] F. Parhami, R.M. McMeeking, A network model for initial stage sintering, Mech. Mater. 27 (1998) 111–124.
[9] R.L. Coble, Sintering of crystalline solids. I. Intermediate and final state diffusion models, J. Appl. Phys. 32 (1961) 787–792.
[10] C.L. Martin, L.C.R. Schneider, L. Olmos, D. Bouvard, Discrete element modeling of metallic powder sintering, Scripta Mater. 55 (2006) 425–428.
[11] B. Henrich, A. Wonisch, T. Kraft, M. Moseler, H. Riedel, Simulations of the influence of rearrangement during sintering, Acta Mater. 55 (2007) 753–762.
[12] S. Martin, M. Guessasma, J. Lchelle, J. Fortin, K. Saleh, F. Adenot, Simulation of sintering using a non smooth discrete element method. application to the study of rearrangement, Comput. Mater. Sci. (84) (2014) 31–39.
[13] J. Rojek, S. Nosewicz, K. Pietrzak, M. Chmielewski, Simulation of powder sintering using a discrete element model, Acta Mech. Autom. 7 (2013) 175–179.
[14] C. Wang, S. Chen, Application of the complex network method in solid-state sintering, Comput. Mater. Sci. 69 (2013) 14–21.
[15] A. Wonisch, T. Kraft, M. Moseler, H. Riedel, Effect of different particle size distributions on solid-state sintering: a microscopic simulation approach, J. Am. Ceram. Soc. 92 (2009) 1428–1434.
[16] A. Wonisch, O. Guillon, T. Kraft, M. Moseler, H. Riedel, J. Rodel, Stress-induced anisotropy of sintering alumina: discrete element modelling and experiments, Acta Mater. 55 (2007) 5187–5199.
[17] T. Rasp, Ch. Jamin, A. Wonisch, T. Kraft, O. Guillon, Shape distortion and delamination during constrained sintering of ceramic stripes: discrete element simulations and experiments, J. Am. Ceram. Soc 95 (2012) 586–592.
[18] C.L. Martin, R.K. Bordia, The effect of a substrate on the sintering of constrained films, Acta Mater. 57 (2009) 549–558.
[19] L. Olmos, C.L. Martin, D. Bouvard, D. Bellet, M. Di Michiel, Investigation of the sintering of heterogeneous powder systems by synchrotron microtomography and discrete element simulation, J. Am. Ceram. Soc. 92 (2009) 1492–1499.
[20] C.L. Martin, H. Camacho-Montes, L. Olmos, D. Bouvard, R.K. Bordia, Evolution of defects during sintering: discrete element simulations, J. Am. Ceram. Soc. 92 (2009) 1435–1441.
[21] S. Nosewicz, J. Rojek, K. Pietrzak, M. Chmielewski, Viscoelastic discrete element model of powder sintering, Powder Technol. 246 (2013) 157–168.
[22] M. Chmielewski, S. Nosewicz, K. Pietrzak, J. Rojek, A. Strojny-Nedza, S. Mackiewicz, J. Dutkiewicz, Sintering behavior and mechanical properties of NiAl, Al_2O_3 and NiAl-Al_2O_3 composites, J. Mater. Eng. Perform. 23 (2014) 3875–3886.
[23] J. Rojek, S. Nosewicz, K. Jurczak, M. Chmielewski, K. Bochenek, K. Pietrzak, Discrete element simulation of powder compaction in cold uniaxial pressing with low pressure, Comput. Particle Mech. 3 (2016) 513–524.
[24] H. Hertz, Uber die beruhrung fester elasticher korper (on the contact of elastic solids), J. Reine Angew. Math. 92 (1882) 156–171.
[25] P. Heitjans, J. Karger, Diffusion in Condensed Matter Methods, Materials Models, third ed., Springer, 2010.
[26] H. Mehrer, Diffusion in Solids - Fundamentals, Methods, Materials, Diffusion-Controlled Processes, Springer Series in Solid-State Sciences, 2007.
[27] A.M. Brown, M.F. Ashby, Correlations for diffusion constants, Acta Metall. 28 (1980) 1085–1101.
[28] W. Gust, S. Mayer, A. Bogel, B. Predel, Generalized representation of grain-boundary self-diffusion data, J. Phys. Colloq. 46 (1985) 537–544.
[29] J.C. Fisher, Calculation of diffusion penetration curves for surface and grain boundary diffusion, J. Appl. Phys. 22 (1951) 74–77.
[30] I. Kaur, Y. Mishin, W. Gust, Fundamentals of Grain and Interphase Boundary Diffusion, Wiley Chichester, West Sussex, 1995.
[31] W.D. Kingery, H.K. Bowen, D.R. Uhlmann, Introduction to Ceramics, second ed., John Wiley and Sons, 1976.
[32] M.N. Rahaman, Ceramic Processing And Sintering, second ed., Marcel Dekker Inc., 2003.
[33] S.J.L. Kang, Sintering: Densification, Grain growth and Microstructure, Elsevier, Amsterdam, 2005.
[34] W.R. Tyson, W.A. Miller, Surface free energies of solid metals: estimation from liquid surface tension measurements, Surface Sci. 62 (1977) 267–276.
[35] M. Methfessel, D. Hennig, M. Scheffler, Calculated surface energies of the 4d transition metals: a study of bond-cutting models, Appl. Phys. A 55 (1992) 442–448.
[36] A.M. Rodriguez, G. Bozzolo, J. Ferrante, Multilayer relaxation and surface energies of FCC and BCC metals using equivalent crystal theory, Surface Sci. 289 (1993) 100–126.
[37] P.S. Kislyi, M.A. Kuzenkova, Role of surface energy in the initial sintering period, Powder Metall. Metal Ceram. 8 (1979) 482–485.

[38] C. Herring, The Physics of Powder Metallurgy, McGraw-Hill Book Co., 1951.
[39] G. Gottstein, L. Shvindlerman, Grain Boundary Migration in Metals, Taylor and Francis, US, 1999.
[40] D.L. Olmsted, S.M. Foiles, E.A. Holm, Survey of computed grain boundary properties in FCC metals: I. Grain boundary energy, Acta Mater. 57 (2009) 3694–3703.
[41] J.K. Mackenzie, Second paper on the statistics associated with the random disorientation of cubes, Biometrika 45 (1958) 229–240.
[42] L.E. Murr, Interfacial phenomena in metals and alloys, Advanced Book Program, Addison-Wesley Pub. Co., 1975.
[43] P.H. Kitabjian, W.D. Nix, Atomic size effects in NiAl based solid solutions, Acta Metall. 46 (1998) 701–710.
[44] S. Frank, S.V. Divinski, U. Sodervall, Ch. Herzig, Ni tracer diffusion in the B2-compound NiAl: Influence of temperature and composition, Acta Mater. 49 (2001) 1399–1411.
[45] Y. Amouyal, E. Rabkin, Y. Mishin, Correlation between grain boundary energy and geometry in Ni-rich NiAl, Acta Mater. 53 (2005) 3795–3805.
[46] G.F. Hancock, B.R. McDonnel, Diffusion in the intermetallic compound NiAl, Phys. Status Solidi (A) 4 (1) (1971) 143–150.
[47] J. Lis, R. Pampuch, Spiekanie, Wydawnictwo AGH, Kraków, 2000 (In Polish).
[48] J.H. Westbrook, R.L. Fleischer, Intermetallic Compounds, Structural Applications of Intermetallic Compounds, vol. 3, John Wiley and Sons, 2000.
[49] C.A. Moose, MS thesis, Pennsylvania State University, 1991.
[50] V. Raghavan, Material Science and Engineering: A First Course, Prentice-Hall of India Pvt. Ltd, 2004.